Acta Oceanol. Sin., 2024, Vol. 43, No. 11, P. 34–44
https://doi.org/10.1007/s13131-024-2397-5
http://www.aosocean.com
E-mail: ocean2@hyxb.org.cn

Understanding the formation mechanism of highly active ridges on East China Sea Shelf during the mid-late Holocene sea-level highstand

Taoyu Xu[1, 2*], Jianxing Liu[1, 2], Shengfa Liu[1, 2], Xisheng Fang[1, 2], Xiaohui Liu[1, 2], Chenguang Liu[1, 2], Chang Zhao[1, 3], Yonghua Wu[1, 2], Zhifang Xiong[1, 2], Yanguang Liu[1, 2], Xuefa Shi[1, 2*]

[1] First Institute of Oceanography, Ministry of Natural Resources, Qingdao 266061, China

[2] Key Laboratory of Marine Geology and Metallogeny, Ministry of Natural Resources, Qingdao 266061, China

[3] Key Laboratory of Marine Science and Numerical Modelling, Ministry of Natural Resources, Qingdao 266061, China

Received 11 October 2023; accepted 15 March 2024

Abstract

Ridges are common features found on continental shelves and understanding their formation processes is crucial for sedimentology, stratigraphy, and geological engineering. This study investigates the development of ridges on the broad shelf of the East China Sea using a core (DH03) and associated seismic profile. Lithology analysis of the core revealed a 50 m thick shallow sandy sequence which consisted mainly of silty fine sands with intercalations of mud beds composed of sand-mud couplets. Benthic foraminifera examination indicated the offshore species were dominant. The seismic profile indicated that the ridges were separated from the older delta layers due to a boundary formed by river erosion during the last glacial maximum. Radiocarbon dating of the sandy sequence revealed an irregular chronological sequence, with most age ranges falling within the past 3 ka. Based on the chronological data from DH03 and other cores, we propose that the ridges, which were formed during the early Holocene transgression, have been active on a shelf scale in the recent 3–2 ka. Synthetic analysis of the shelf-scale ridge formation processes indicates that the sea-level fluctuations during the mid-late Holocene sea-level highstand triggered the ridge activities. A center for ridge activity developed in the southern shelf, facilitated by thicker ridge deposits in the paleo-Changjiang River Estuary and stronger currents (tidal currents and possibly internal waves) induced by the remaining funnel-shaped estuary topography. Based on these findings, we propose a conceptual model for ridge development, which includes a ridge formation stage during the early Holocene transgression and a ridge activation stage during the mid-late Holocene sea-level highstand.

Key words: seabed ridge, ridge activity, mid-late Holocene, outer shelf, East China Sea

Citation: Xu Taoyu, Liu Jianxing, Liu Shengfa, Fang Xisheng, Liu Xiaohui, Liu Chenguang, Zhao Chang, Wu Yonghua, Xiong Zhifang, Liu Yanguang, Shi Xuefa. 2024. Understanding the formation mechanism of highly active ridges on East China Sea Shelf during the mid-late Holocene sea-level highstand. Acta Oceanologica Sinica, 43(11): 34–44, doi: 10.1007/s13131-024-2397-5

1 Introduction

The continental shelves worldwide exhibit diverse sediment distribution and seabed topography due to distinctive hydrodynamic processes (e.g., waves, marine currents, and gravity flows) operated with glacial-eustasy during the Quaternary period (Masson et al., 2003; Sun et al., 2022; Liu et al., 2022; Wang et al., 2023; Wu et al., 2023). The ridge-and-swale topography, which is mainly composed of sand, is a common feature found on modern continental shelves (Amos and King, 1984; Dyer and Huntley, 1999; Snedden and Dalrymple, 1999). Understanding the processes that form these ridges is important for the fields of sedimentology, stratigraphy, and geological engineering (Yang, 1989; Berné et al., 2002; Snedden et al., 2011).

The East China Sea (ECS) is characterized by a broad and gently sloping shelf (Fig. 1; Liu et al., 2003). The outer shelf is covered by extensive ridges, with water depths ranging from approximately 60 m to 100 m (Li et al., 2014). Over the past 50 years, numerous studies have been conducted on the evolution of these ridges using core and seismic profiling data (Yang, 1989; Saito et al., 1998; Berné et al., 2002; Yang et al., 2001; Chen et al., 2003; Yin, 2003; Liu et al., 2007, 2020; Wu et al., 2010). An initial study by Yang (1989) reported that the sandy ridges exhibit a northwest-southeast orientation, with southwest-dipping layers, and were unconformably underlain by estuarine and fluvial sediments. Thus, the ridges were suggested to form by tidal current acting on pre-existing deposits in a paleo-estuary with the post-glacial (early Holocene) transgression. However, the ridges stopped growing and became inactive under the mid-late Holocene highstand of sea level (since ~7 ka) (Yang, 1989). A later study by Saito et al. (1998) analyzed radiocarbon ages of core samples and concluded that the tidal ridges were formed in open offshore environments during the post-glacial transgression. They were subsequently abandoned when the sea level reached its highstand during the mid-late Holocene. Yang et al. (2001) further noted that the development of ridges was favored only during a decelerated rise or short-term stillstand of the sea level.

Foundation item: The National Natural Science Foundation of China under contract No. T2192951; the Basic Scientific Fund for National Public Research Institutes of China under contract Nos 2021Q09 and 2021S01.
*Corresponding author, E-mail: xuty@fio.org.cn; xfshi@fio.org.cn

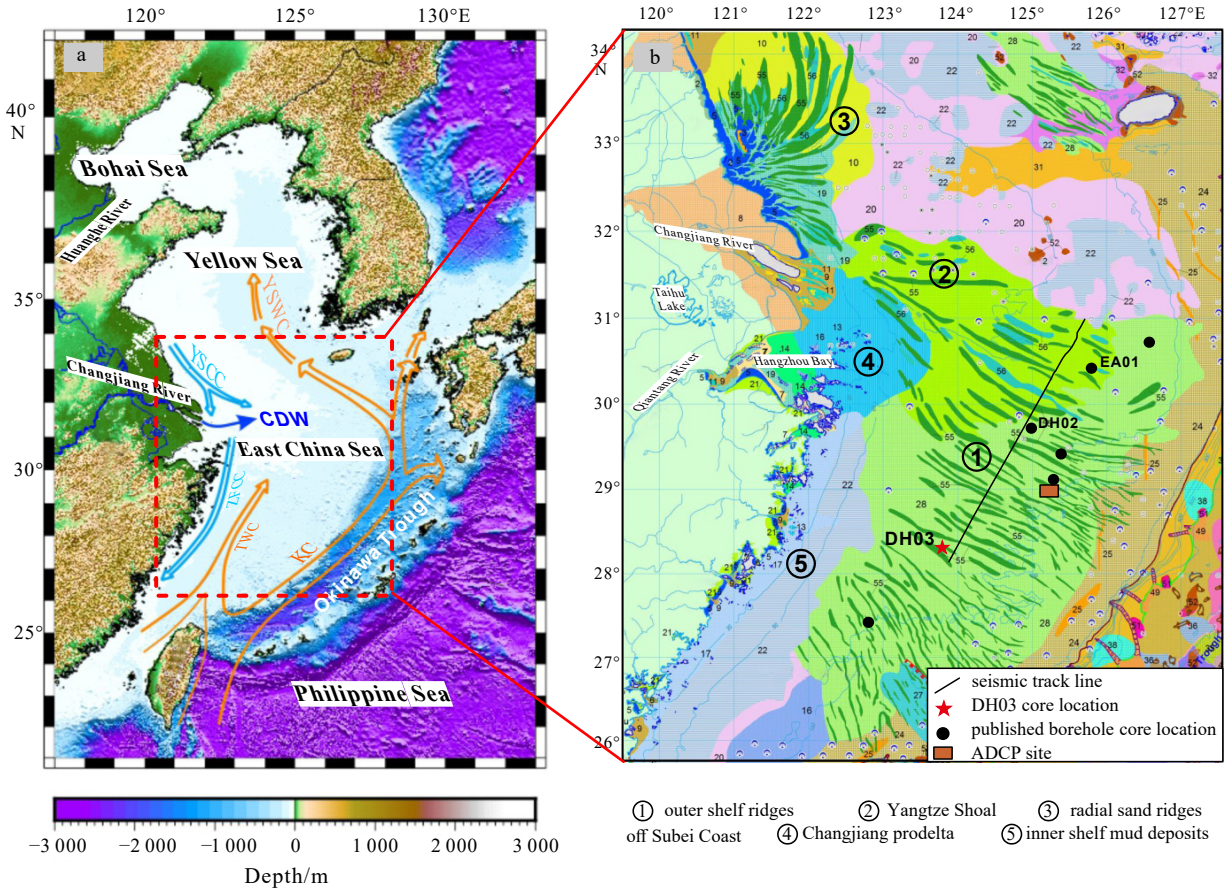

Fig. 1. Sketch map of study area. a. Regional geological setting and oceanic circulation [modified from Liu et al., (2021)]. Red dashed square demarcates the study area. Other map features include the Yellow Sea Coastal Current (YSCC), Zhejiang–Fujian Coastal Current (ZFCC), Yellow Sea Warm Current (YSWC), Changjiang River Diluted Freshwater Plume (CDW), Kuroshio Current (KC), and Taiwan Warm Current (TWC); b. Specific topography, sedimentary patterns, bathymetric contours (m) (modified from Li et al., 2014), as well as locations of seismic profile and borehole cores, including DH03, the collected DH02 (Xu et al., 2020), EA01 (Li et al., 2002) and other previously published core sites. Acoustic Doppler Current Profiling (ADCP) site was denoted according to Berné et al. (2002).

Rapid sea-level rise, on the other hand, led to the landward migration of the ridge field. Wu et al. (2010) categorized the periods of ridge formation based on the incremental rise in sea level following the last glacial maximum (LGM). Some studies also suggested that erosional tidal ridges initially formed in the paleo-estuary and then served as precursors for the formation of depositional tidal ridges in offshore environments during further transgression (Berné et al., 2002; Chen et al., 2003). A comprehensive analysis of ridge distribution on the ECS shelf proposed that the spatial patterns of ridges are linked to their formation in near-estuary or offshore regions (Wu et al., 2010).

In contrast to the aforementioned studies that insist on the understanding of moribund or abandoned ridges, Yin (2003) suggested that seabed ridges may still be undergoing active processes based on field tests of seabed tidal currents. Building upon this idea, Liu et al. (2007) identified a limited number of young radiocarbon ages (less than 2 ka) in the near-seabed ridge layer and defined ridges as quasi-active, indicating that they exhibit minor activity in the modern seabed. This perspective has been widely accepted by recent Quaternary sedimentary studies (Wang et al., 2014, 2022). Additionally, Liu et al. (2020) studied the formation of the Yangtze Shoal and found that the tidal ridges in the Changjiang River Estuary transformed into flat sand banks due to local rotary tidal currents during the mid-late Holocene sea-level highstand.

In the past five decades, numerous scientific studies have significantly advanced our understanding of the formation and evolution of shelf ridges in the ECS. However, there are still notable limitations in our knowledge due to the uneven distribution of borehole cores, which are primarily concentrated in the northern regions of the shelf. As a result, the southern area has received limited attention and data. Recently, we acquired a long core, DH03, approximately 100 m in length, from the ridge fields in the southern ECS shelf. The core exhibits a remarkably thick sandy sequence, measuring 50 m, compared to the previous cores where the corresponding sand bed is commonly less than 20 m thick. In this study, our focus is on understanding the formation mechanism of this unusually thick sandy sequence using core DH03 and an associated seismic profile. Firstly, we conducted a comprehensive analysis of the lithology, microfossil (benthic foraminifera assemblage), and chronology. Secondly, we interpreted the stratification by comparing the seismic profile with nearby cores. Thirdly, we will analyze the sedimentary formation processes around the ridge activities under the mid-late Holocene sea-level highstand based on core sediment characteristics. Finally, we will develop a model for the formation of ridges in the ECS shelf based on the combined evidence from the core and seismic data.

2 Regional setting

The ECS is a Pacific marginal sea located at the junction of the Eurasian and Pacific Plates, covering an area of 773 000 km^2 (Liu et al., 2000). The ECS is primarily comprised of a continental shelf region and the Okinawa Trough. The continental shelf, which accounts for over 66% of the ECS, is one of the largest in the world, with a distance of at least 600 km from the coastline to the shelf break (Fig. 1; Berné et al., 2002; Yang et al., 2015).

The ECS shelf has been topographically divided into two parts comprising inner and outer shelves with a boundary at a water depth of ~60 m (Li, 2008). The inner shelf is covered by the delta-related muds, while the outer shelf is characterized by widespread, large, elongated ridges that are several kilometers wide, 10–60 km long, and ⩽20 m thick (Yang, 1989). These ridges occur in groups, parallel to each other, and extend in the NW-SE direction, following the direction of tidal currents. Seasonal monsoon climates are in effect, with summer monsoons blowing landward from the sea, whereas winter monsoons show reverse directions.

The ECS is hydrodynamically dominated by a tidal current facilitated via the wide gentle shelf topography (0.28‰; Liu et al., 2003; Berné et al., 2002). The great axis of the tidal ellipse is oriented from NW to SE, with the maximum flood and ebb currents flowing toward the former and the latter, respectively. The tidal range is >5 m in height, while the normal wave base lies ~10 m below sea surface (Wang et al., 2005). The ECS is subject to two to three annual typhoons (mainly in August to September) deriving from the equatorial zone of the SW Pacific (Sun et al., 2013; Cao et al., 2023). The ECS oceanic current system is dominated by the northward intrusion of the Kuroshio Current, its branch (the Taiwan Warm Current), and the southward Zhejiang–Fujian Coastal Current, which prevails in winters and is related to southward blowing NE monsoonal winds (Yang et al., 2015). During the summer, Changjiang River Diluted Water plays an important role in the shelf circulation of the northern ECS (Liu et al., 2006).

3 Materials and methods

3.1 *Core DH03 analyses*

The core DH03 is located in the ridge fields of the southern outer shelf of the ECS (28°18′N, 123°48′E). The core was drilled using a cord hammer coring method by R/V *Kan 407* in September 2015 (Fig. 1). It has a total length of 101.6 m and a recovery rate of 81.6%.

For grain size measurements and microfossil examinations, sediment samples with a thickness of 2 cm were collected from the upper sandy succession (0–48.2 m in core depths) at intervals of approximately 10 cm and 50 cm, respectively. A total of 352 samples were collected for grain size analysis, while 81 samples were collected for microfossil assemblage examination. It is worth noting that these core samples have previously undergone testing and analysis in a magnetic study conducted by Liu et al. (2021), albeit with limited mention.

Six well-preserved subsamples of benthic foraminifera were subjected to ^{14}C dating using the accelerator mass spectrometry (AMS) method by Beta Analytic Inc. Prior to dating, the subsamples underwent physical abrasion to eliminate external surfaces and any carbonate material adhering to them. Subsequently, acid etching was performed to remove approximately 10%-30% or more of the total weight, ensuring that only the reliable primary carbonate was dated. Following the pre-treatment, all samples used for age determination weighed more than 4 mg, meeting the minimum threshold for dating. Each of the six radiocarbon ages (Table 1) were corrected for the regional marine reservoir effect [(165 ± 30) a; Yoneda et al., 2007], and calibrated using CALIB810 (http://calib.org/calib/download/). The calibrated ages were reported as calendar ^{14}C ages before 1950 CE, with one standard deviation (1σ) uncertainty (Table 1). The 13 collected dates [including seven of DH03 cited from Liu et al. (2021) and six of DH02 cited from Xu et al. (2018)] were calibrated via the method introduced in this study.

3.2 *High-resolution seismic data*

A seismic profile oriented in the NE-SW direction and spanning approximately 350 km was collected by the Chinese–French marine geology and geophysics investigation during a cruise of the French R/V *L'Atalante* in 1996 (Fig. 1). The data was acquired using a SIG sparker with a frequency range of 200-600 Hz and an energy output of 700 J. The shooting interval was set at 1 s or 2 s, while the speed of this ship during data acquisition was approximately 6 kn.

The seismic profile was previously used to analyze the sequence framework (Xu et al., 2020). However, in this study, the top sandy portion of the profile was reinterpreted based on the newly drilled borehole core DH03. To calculate water depth and sediment thickness, an assumed acoustic velocity of 1 600 m/s was used, consistent with previous studies conducted on the ECS shelf (Liu et al., 2000; Xu et al., 2020).

4 Results

4.1 *Synthetic characteristics of DH03 (lithology, microfossil, and chronology)*

The upper sandy section of DH03, spanning from 0 m to 48.2 m in core depth (Figs 2, 3a–z), was observed to unconformably overlay a uniform mud sequence (Figs 2, 3z–aa). This mud sequence originates from prodelta deposits of Marine Isotope Stage 3 (MIS 3), which occurred between 35 ka and 50 ka (Berné et al., 2002; Liu et al., 2021; Pico et al., 2017). An internal erosion surface observed at 24.77 m divided the upper section of DH03 into two depositional units, referred to as DUs 1 and 2 in descending order (Fig. 2). In the following sections, we provided a detailed analysis of the lithology changes, sedimentary structure, grain-size composition, and benthic foraminifera assemblages for each of these units.

4.1.1 *DU2 (24.77–48.2 m)*

This unit exhibited an erosional base (Figs 3z–aa). It comprised greenish grey silty fine sands, with frequent alternating muddy beds exhibiting lenticular or flaser bedding structures. Millimeter-scale shell debris and mud pebbles scattered (Figs 2, 3n–z). The basal section (44.3–48.2 m) contained a mixture of sands and abundant shell debris (maximum diameter, ~4 mm; Figs 2, 3y–z).

Grain-size analysis revealed a dominant sand component (17.88%–98.21%; mean, 78.74%), followed by silts (1.79%–69.17%; mean, 18.65%) and clays (0–16.02%; mean, 2.60%; Fig. 2). The mean grain size ranged from φ1.58 to φ5.73 (mean, φ3.10) (Fig. 2).

The benthic foraminifera in this unit exhibited species numbers ranging from 0 to 54.00 (mean, 16.85) and total abundances ranging from 0 to 36 216.37 pieces/(50 g) [mean, 3 484.03 pieces/(50 g); Fig. 4]. Relict (broken) benthic foraminifera were widespread, with an average content of 39.93%. The dominant assemblage of benthic foraminifera consisted of outer-shelf species (0–81.0%; mean, 26.42%), while the other two species types

Table 1. ^{14}C dates of borehole cores DH03 and DH02

Core	Core depth/m	Material	Species	Convention ^{14}C age/(a BP)	$\delta^{13}C$/‰	Calibrated age/(a BP)		Lab code No.	Data source
						Median	Range (1σ)		
DH03	0.54	BF	*Ammonia compressiuscula, Pseudorotalia indopacifica*	3 920 ± 30	0	3 420	3 339–3 500	Beta459495	This study
	2.83	BF	*Ammonia compressiuscula, Pseudorotalia indopacifica*	2 580 ± 30	0.2	1 781	1 697–1 864	Beta459498	This study
	3.65	BF	*Ammonia compressiuscula, Pseudorotalia indopacifica, Rectuvigerina* sp.	2 650 ± 30	−0.3	1 878	1 791–1 965	Beta459496	This study
	8.59	BF	*Ammonia compressiuscula, Pseudorotalia indopacifica*	3 560 ± 30	0.6	2 961	2 868–3 054	Beta459497	This study
	10.72	BF	*Ammonia compressiuscula, Pseudorotalia indopacifica*	3 750 ± 30	−0.1	3 233	3 145–3 320	Beta459499	This study
	18.67	BF	*Ammonia compressiuscula, Cavarotalia annectens, Elphidium* spp., *Quinqueloculina tikutoensis Nakamura*	2 920 ± 30	−0.5	2 220	2 137–2 302	Beta459500	This study
	0.74	BS	*Pecten albicans*	9 180 ± 30	1.0	9 445	9 375–9 514	Beta466865	Liu et al. (2021)
	5.47	BF	*Pseudorotalia indopacifica, Rotalinoides compressiuscula, Lenticulina* sp.	3 770 ± 30	0.3	3 252	3 167–3 336	Beta459494	Liu et al. (2021)
	11.45	BF	*Pseudorotalia indopacifica, Rotalinoides compressiuscula, Quinqueloculina bicostata*	3 090 ± 30	0.1	2 413	2 323–2 503	Beta466866	Liu et al. (2021)
	19.20	BS	*Veneridae* or *Crassatellidae*?	9 550 ± 30	1.1	9 918	9 797–10 039	Beta466867	Liu et al. (2021)
	29.40	BF	*Pseudorotalia indopacifica, Rotalinoides compressiuscula*	3 470 ± 30	−0.1	2 857	2 774–2 939	Beta466868	Liu et al. (2021)
	38.70	BF	*Pseudorotalia indopacifica*	2 950 ± 30	0.6	2 228	2 146–2 310	Beta466869	Liu et al. (2021)
	43.81	BF	*Pseudorotalia indopacifica, Lenticulina* sp.	2 880 ± 30	0.6	2 149	2 053–2 245	Beta517586	Liu et al. (2021)
DH02	0.39	BF	*Pseudorotalia indopacific, Rotalinoides compressiuscula, Ammonia* spp., *Rotalidium annectens*	3 350 ± 30	−0.5	2 758	2 685–2 831	Beta472416	Xu et al. (2018)
	2.46	BF	*Pseudorotalia indopacific, Rotalinoides compressiuscula, Ammonia* spp., *Quinqueloculina* spp., *Spiroloculina* sp.	3 930 ± 30	−0.6	3 444	3 362–3 525	Beta472427	Xu et al. (2018)
	2.53	BF	*Pseudorotalia indopacific, Rotalidium annectens, Ammonia* spp., *Quinqueloculina* spp.	2 240 ± 30	−0.5	1 399	1 323–1 474	Beta472429	Xu et al. (2018)
	4.56	BF	*Rotalinoides compressiuscula, Ammonia* spp., *Quinqueloculina* spp.	6 150 ± 30	0.1	6 119	6 028–6 209	Beta472428	Xu et al. (2018)
	8.49	BF	*Pseudorotalia indopacific, Rotalidium annectens, Quinqueloculina* spp.	3 250 ± 30	1	2 614	2 525–2 703	Beta472431	Xu et al. (2018)
	8.58	BF	*Pseudorotalia indopacific, Rotalidium annectens, Ammonia* spp., *Quinqueloculina* spp.	2 790 ± 30	0.2	2 035	1 946–2 124	Beta480425	Xu et al. (2018)

Note: Median value of the calibrated age was an integer number of calculation results, which was processed through rounding. BF: benthic foraminifera; BS: bivalve shell.

were less common (inner-shelf species: 0.00–33.33%; mean, 4.67%, and euryhaline-brackish species: 0.00–33.33%; mean, 3.44%; Fig. 4). The most representative benthic foraminifera species was *Bolivina robusta* (mean, 8.00%) from the outer-shelf species (Fig. 4).

4.1.2 *DU1 (0–24.77 m)*

This unit exhibited sediment characteristics similar to DU2, including an erosional base, lithological succession, and sedimentary structures (Figs 2, 3a–n).

Grain size analysis revealed that sand components were dominant (3.14%–95.74%; mean, 72.80%), followed by silt (3.86%–73.01%; mean, 23.19%) and clay components (0–25.41%; mean, 4.01%; Fig. 2). The mean grain size ranged from φ1.82 to φ6.98 (mean, φ3.58).

Among the microfossils present in this unit, the total abundance [0–116 722.47 pieces/(50 g), mean 10 961.90 pieces/(50 g)] and number of species (0–58.00; mean, 31.15) generally increased upwards with significant fluctuations (Fig. 4). A large amount of relict benthic foraminifera was found in the bottom section (20.80–24.77 m), with a mean content of 11.78% (Fig. 4). The benthic foraminifera assemblage was dominated by outer-shelf species (0–77.58%; mean, 35.16%), while euryhaline-brackish species (0–70.37%; mean, 15.42%) and inner-shelf species (0–36.04%; mean, 11.34%) were less common (Fig. 4). The most typical benthic foraminifera species was *Bolivina robusta* (mean, 10.03%) among the outer-shelf species.

Six newly conducted ^{14}C dating analyses on benthic foraminifera subsamples at core depths of 0.54 m, 2.83 m, 3.65 m, 8.59 m, 10.72 m, and 18.67 m yielded dates of 3.4 ka, 1.8 ka, 1.9 ka, 3.0 ka, 3.2 ka, and 2.2 ka, respectively (Fig. 2; Table 1).

4.2 *Interpretation of the seismic profile*

In the NE-SW oriented seismic profile (Fig. 5a), the seabed displayed ridge-and-swale topography with vertical fluctuations of less than 20 m. The ridges in the southern region exhibited sharp shapes, while the ridges in the northern region had more gentle shapes (Fig. 5b). The seismic profile was located in close proximity to three cores, namely DH03, DH02 (Xu et al., 2020), and EA01 (Fig. 5b; Li et al., 2002), with the former two cores slightly east and west of the seismic line. To establish the core-seismic correlation, we projected the borehole positions onto the seismic profile, following the methodology of Harding et al. (2016) (Fig. 5b). By comparing the seismic units with the three nearby cores (Figs 5b and c), we identified a distinct surface, named R1, which separated the upper seismic unit (SU) 1 of sandy sediments from the lower SU2 of muddy sediments with delta progradation structures.

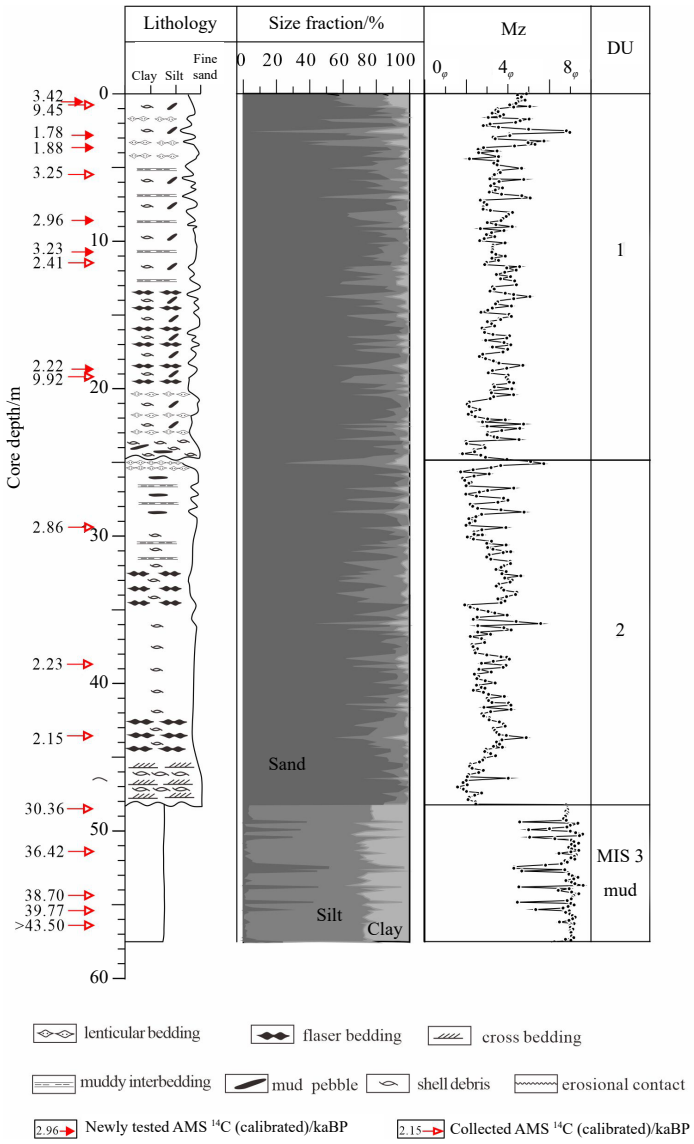

Fig. 2. Composite column of core DH03 showing AMS ^{14}C dating, lithology, grain-size composition, mean grain size (Mz) and deposition units (DUs). The grain-size parameters and five ^{14}C ages from the deeper muds were adapted from Liu et al. (2021). MIS: marine isotope stage.

The surface, R1, was traced over the seismic profile (Fig. 5a). It was uneven and gradually declined in depth towards the south. It truncated the underlying SU2 with progradation structures. In the northern part, R1 had an elevation of approximately 80 m below sea level, while in the southernmost point, it reached elevations of around 150 m below sea level (Fig. 5a). The southern section of R1 had a valley-like shape, previously identified as the base of mid-Quaternary strata (Xu et al., 2020). The previous understanding of R1 has been revised. It is now interpreted as a river erosion surface (RES) that occurred during the LGM, which is comparable to a sequence boundary in sequence stratigraphy. This new interpretation is consistent with the understanding of the northern section of R1 which is supported by additional core data (e.g., DH02 and EA01) (Figs 5b and c).

The deeper SU2, located below R1, was typical of MIS 3 delta strata characterized by the shelf-scale progradation structures (Figs 5b and c). The near-seabed SU1, developed unevenly consistent with the occurrences of the basal surface R1 (Fig. 5b). In the northern part, SU1 had a thickness of less than 20 m, and the shallowest sections were well-stratified with dipping layers. In contrast, the sandy strata in the southern depressed areas were much thicker (up to approximately 70 m) and displayed faint reflections (Figs 5a and b). The internal erosion surface observed in SU1 of DH02 and DH03 (Fig. 5b), which separates the upper sandy succession into two or three parts, was not identified in the seismic profile, likely due to its relatively low resolution.

5 Discussion

5.1 *Shelf-scale ridge activities under sea-level highstand of recent 3–2 ka*

Seismic-core correlation shows that the upper sandy part of DH03 corresponds to the seabed ridge (Fig. 5), while the underlying muddy part represents the delta of MIS 3 that developed on the shelf with a progradation structure (Liu et al., 2003; Berné et al., 2002). A total of 13 radiocarbon ages were obtained from the ridge succession of DH03 (Fig. 2; Table 1). Out of these ages, eleven were obtained from well-preserved benthic foraminifera

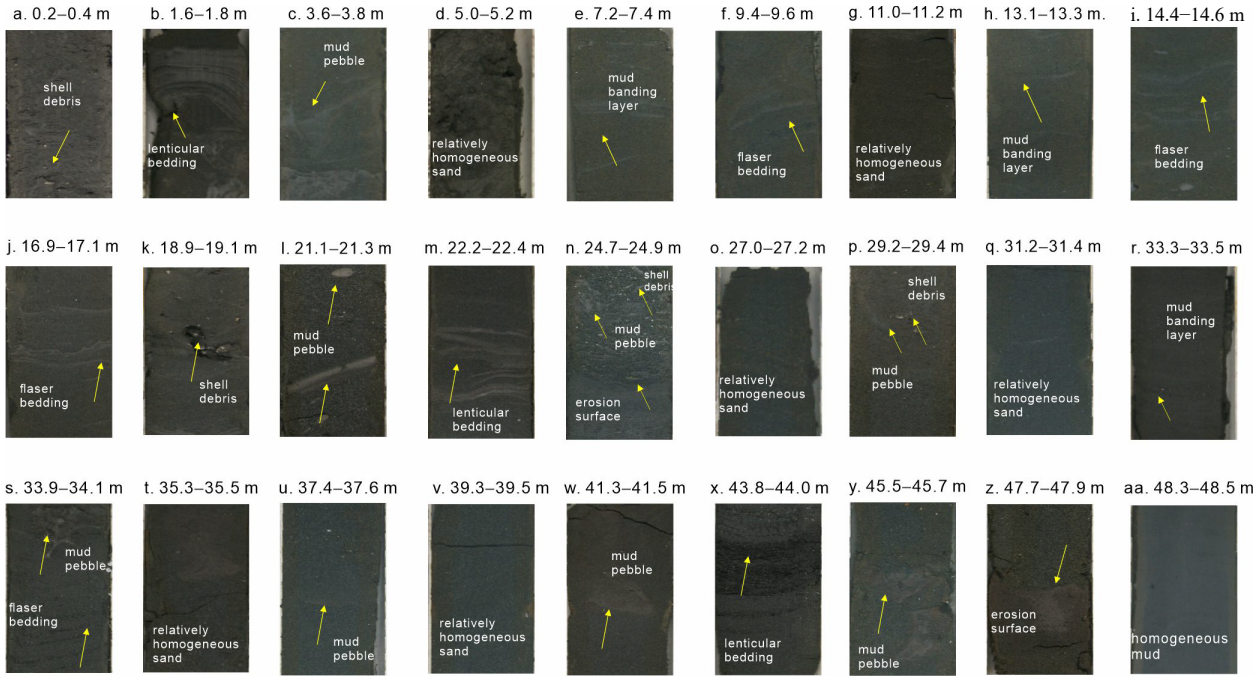

Fig. 3. Photographs of representative lithological features and sedimentary structures in core DH03. Yellow arrows indicate distinct sedimentary structures.

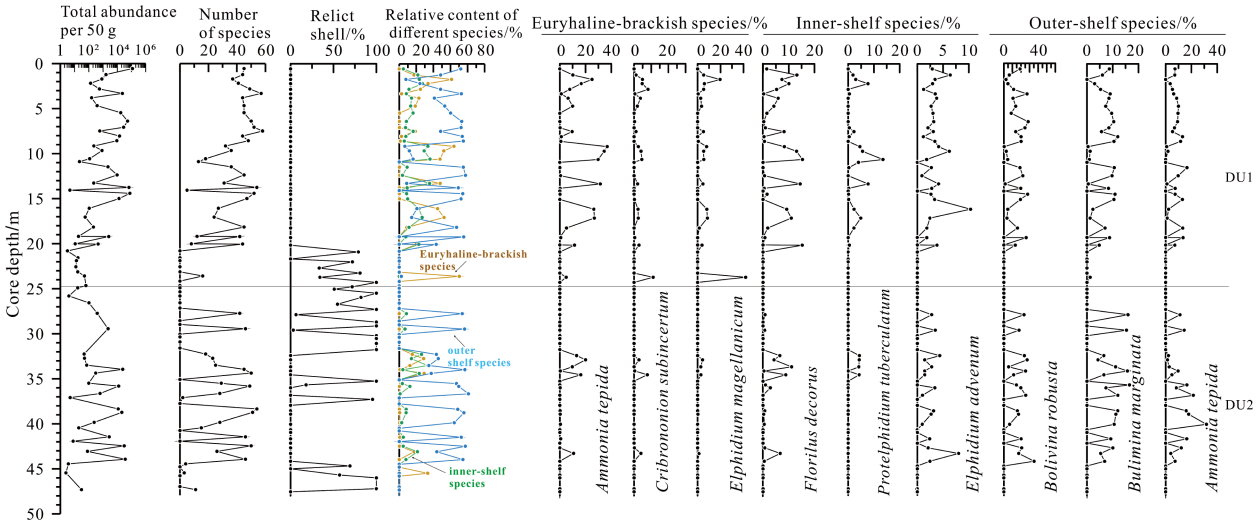

Fig. 4. Downcore distributions of abundance and species number for benthic foraminiferal assemblages in core DH03.

subsamples, indicating a narrow time range of 1.8–3.4 ka within the late Holocene. Similarly, in the northward core DH02, all six ages of its thinner ridge record also indicate a relatively narrow time range of 1.4–6.1 ka within the mid-late Holocene (Fig. 5c). However, these mid-late Holocene ages contradict the established mode of ridge formation, which suggests that the ridges were formed by tides during the post-glacial (early Holocene) transgression (Yang et al., 2001; Liu et al., 2007; Berné et al., 2002; Li et al., 2014; Liu et al., 2020). Under the mid-late Holocene sea-level highstand since 7 ka (Fig. 6), an equilibrium was considered to have been established between the tidal current field and the development of tidal sand ridges in response to limited sediment supplies and weakened tidal currents. However, the ridge formation mode only agrees with the remaining two ages of DH03 obtained from shell debris which suggests much older date of approximately 10 ka (Fig. 2; Table 1). The combination of these findings in the two cores DH03 and DH02 suggests that some mid-late Holocene materials have been added to the early Holocene tidal ridges.

Liu et al. (2007) also observed young radiocarbon ages (less than 2 ka) in the near-seabed layers of the ridges in two gravity cores from the ridge field of outer ECS shelf. It was suggested that the ridges are currently quasi-active, with slight activity limited to the thin layer near the seabed (Liu et al., 2007). *In-situ* ADCP tests (Fig. 1b) support this conclusion, showing near-bed current velocities of up to 0.55 m/s under fair weather conditions at a water depth of 90 m (Berné et al., 2002; Yin, 2003; Liu et al., 2007). These tidal currents can move unconsolidated sand particles. However, the lower sections of the gravity cores also showed young radiocarbon ages, and the reason for this phenomenon

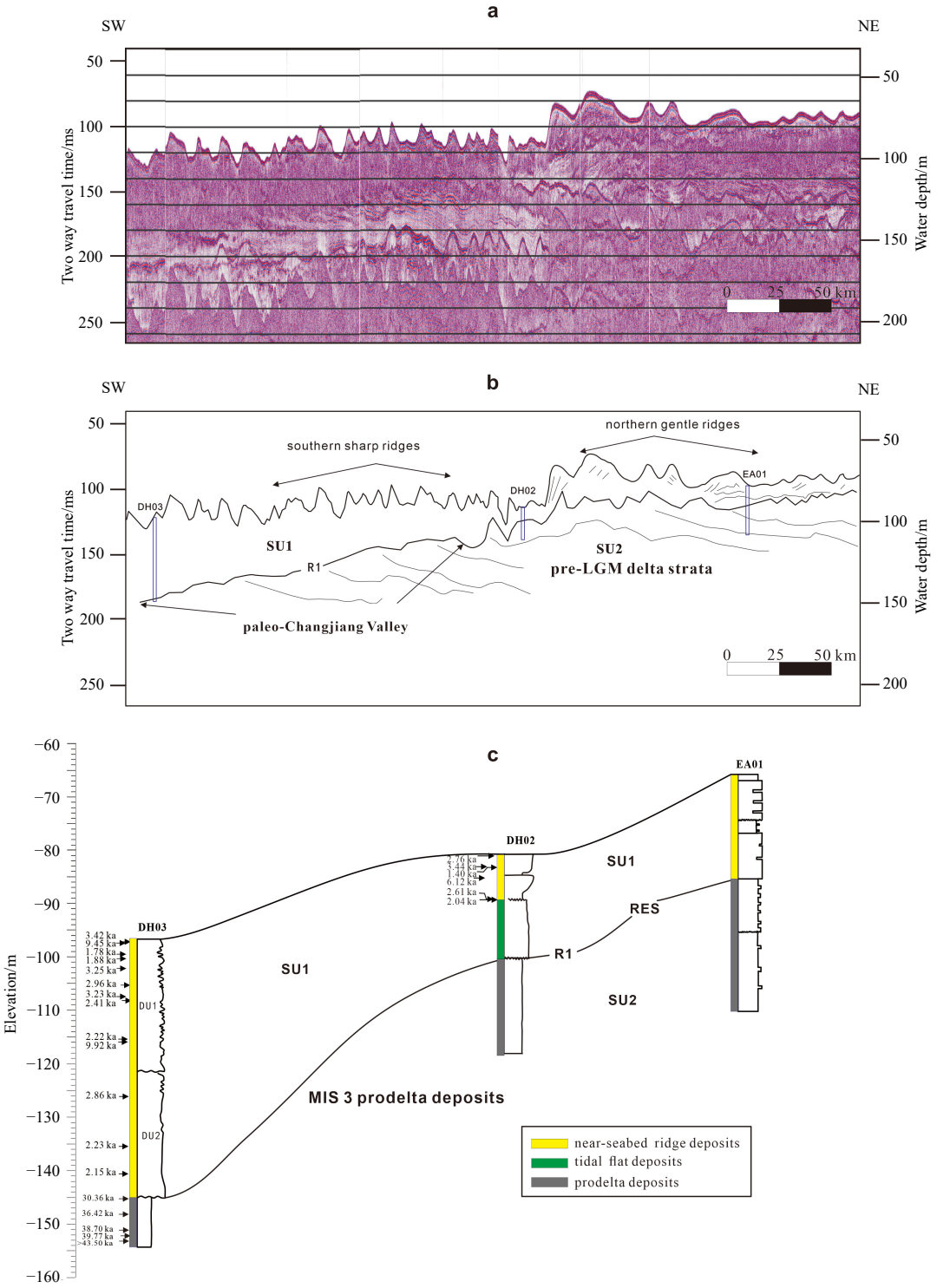

Fig. 5. The raw seismic profile (a); the interpreted seismic profile [modified from Xu et al. (2020)] and projected positions of borehole cores (b); core successions of DH03, DH02 [modified from Xu et al. (2020)] and EA01 [modified from Li et al. (2002)] (c). RES: river erosion surface. See Fig. 1b for the locations of seismic track lines and boreholes.

was not explained in the relevant studies (Saito et al., 1998; Liu et al., 2007). Additionally, Liu et al. (2020) discovered that the early Holocene tidal ridges in the landward offshore area of the modern Changjiang River Estuary have transformed into sheet-like sand banks (Yangtze shoal, Fig. 1b) due to local rotary tidal currents.

Overall, the chronological data from cores DH02 and DH03, as well as previous cores, suggest that the ridges, which formed during the early Holocene transgression, have been active on a shelf scale within the past 3–2 ka. Particularly, the disordered chronology of the two long cores DH03 and DH02 indicates that the ridge activity is not limited to the seabed layer but has extended throughout the entire ridges, which can be several tens of meters thick. This implies a rapid and intensified ridge

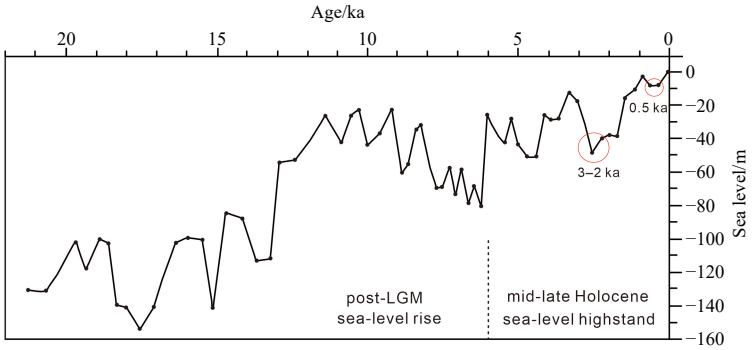

Fig. 6. Post-LGM sea-level curve of the East China continental shelf [modified from Qian (1996) and Yang et al. (2001)].

activity.

5.2 *Mid-late Holocene sea-level fluctuations triggered ridge activities on the shelf scale*

During the late Quaternary, the ECS shelf has a relatively stable tectonic background (Berné et al., 2002). The primary factor influencing sedimentary activities on the shelf was the variations in sea level stands. The rise of sea level during the early Holocene caused the landward migration of ridges over the ECS shelf (Yang et al., 2001; Liu et al., 2007, 2020). During the mid-late Holocene, the sea level also fluctuated between 10 m and 30 m during its highstand (Fig. 6; Qian, 1996; Yang et al., 2001). Particularly, a recent significant sea-level decline of ~30 m occurred at 3–2 ka (Fig. 6). Such huge sea-level decline could disrupt the equilibrium between sea level and ridge field development (Berné et al., 2002; Liu et al., 2007), leading to the activation of the ridges and the establishment of a new equilibrium. Borehole core records with two depositional units indicate two distinct stages of ridge activity since 3–2 ka. A less significant sea-level decline of 10 m around 0.5 ka (Fig. 6) likely triggered the most recent ridge activities. Consequently, the records of the previous ridge activity stage between 3 ka and 0.5 ka unconformably overlain those of recent stage from 0.5 ka.

The sedimentary processes with ridge activities were mainly driven by the ebb-dominated tidal currents, with a secondary tidal current flowing southwest in a perpendicular direction to the main flow (Liu et al., 2007). These currents caused lateral movement of sediment particles, resulting in erosion and transport of sand particles and shell debris towards the lee slope of existing ridges. As a result, new layers were deposited unconformably on top of older inclined layers (Yang et al., 2001; Liu et al., 2007). This repetitive process led to a reversal or disordering of the chronological order. With the ridge activity, seabed topography changed, alternating between crest and swale (Yang et al., 2001). This created sedimentary cycles characterized by vertical alternations of sandy and muddy beds (Figs 2 and 3; Yang et al., 2001). The alternating layers of sand and mud in the muddy beds are formed due to the fluctuating tidal currents. In addition, frequent minor fluctuations in sea level also likely influenced the sedimentary cycles (Fig. 6). Occasionally, hydrodynamic events such as typhoons and winter storms had destructive effects, but these were often erased by the persistent tidal currents (Zhang et al., 1999). It is important to note that the persistent sea-level fluctuations during the highstand period since 7 ka likely caused repeated stages for ridge activities. Modern seabed ridges can only provide evidence of the most recent one or two activity stages due to the deposition of more recent materials. The reduced presence of shell debris in the top unit of the ridge in DH03 (Fig. 4) suggests a decline in ridge activity. This is probably because the ridge topography and tidal current patterns have reached a balance in response to the relatively stable sea level in recent 0.5 ka (Fig. 6).

5.3 *Ridge activity center in the paleo-Changjiang River Estuary*

The seismic profile and borehole cores indicate the presence of a ridge activity center in the southern shelf of the ECS, near the DH03 site (Fig. 5). This center is characterized by a ridge that is approximately 50 m thick, which is significantly thicker than the ridges in the rest of the northern shelf (Fig. 5). The base of the ridge at the DH03 site, known as R1, is merged with river incision base of the LGM, suggesting the existence of a paleo-Changjiang River valley (Uehara and Saito, 2003; Wellner and Bartek, 2003; Li et al., 2014). The current shape of the 50 m isobath in the modern seabed reflects the remaining outline of the paleo-Changjiang River Estuary that likely prevailed during the Younger Dryas period around 12 ka (Fig. 1b; Li et al., 2014).

The paleo-estuary, with its large space and abundant sediment supply, played a crucial role in the formation of thick strata, which is a key prerequisite for the formation of the ridge depocenter during subsequent sea-level rise and the highstand of the post-glacial period. A stronger tidal current is also necessary. The funnel-shaped topography of the paleo-estuary facilitates the convergence of currents, contributing to a stronger tidal current with post-glacial sea-level rise (Uehara and Saito, 2003). The modern V-shaped topography of the remaining estuary enhances tidal currents under sea-level highstand and triggers internal waves (Fang et al., 1989; Jiang and Lü, 2007). This further intensifies the currents (Reeder et al., 2011; Wang et al., 2020). The significant difference in hydrodynamic intensities between the southern and northern shelves of the ECS is evidenced by the contrasting seabed topography of the ridges. The southern ridges are sharp, while the northern ridges are gentle (Fig. 5a).

In summary, the presence of the paleo-Changjiang River Estuary in the southern ECS shelf determines the ridge activity center due to the combination of two factors: the thicker strata and the stronger hydrodynamic forces.

5.4 *Synthetic mode of ridge evolution*

Based on the findings of this study, a conceptual mode for the evolution of ridges in two stages is established here (Fig. 7).

5.4.1 *Ridge formation during the early Holocene transgression*

During the deglacial transgression, the valley that had incised the outer shelf during the LGM became flooded, forming a tide-

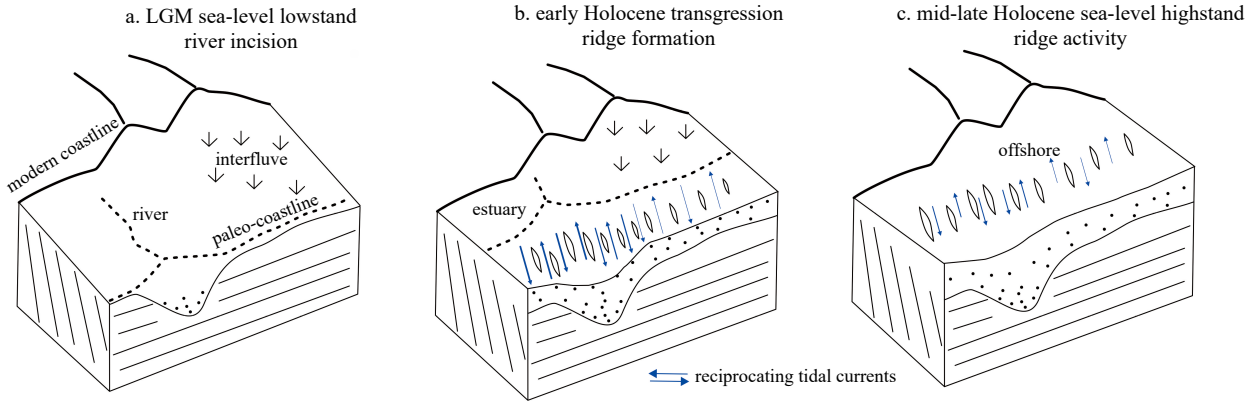

Fig. 7. Sketch mode showing the staged development of the ridges in the ECS shelf. The Changjiang River valley incised the shelf during the sea-level lowstand around the LGM (a); tidal ridges formed during early Holocene transgression (b); ridge activated during the mid-late Holocene sea-level highstand (c).

dominated estuary (Figs 7a and b). Thicker layers of sediment, such as river and tidal flat deposits, accumulated within the estuary due to the ample space and sediment supply. Tidal currents eroded the shelf deposits, particularly within the estuary where currents were intensified by the funnel-shaped topography (Fig. 7b; Chen et al., 2003; Uehara and Saito, 2003). With the further transgression during the early Holocene, the existing uneven seabed features, known as erosional ridges, served as precursors for the formation of tidal sand ridges in the offshore environment (Berné et al., 2002; Chen et al., 2003). The ridge formation favored an optimum water depth of about 30 m during the deceleration of sea-level rise (Yang et al., 2001; Liu et al., 2007). As sea levels continued to rise, the ridge field migrated landward over the ECS shelf.

5.4.2 *Ridge activation during the mid-late Holocene sea-level highstand*

During the sea-level highstand of the mid-late Holocene, which began around 7 ka (Fig. 6), the shelf remained in offshore environments (Fig. 7c), with small-scale fluctuations in sea level. Tidal currents continued to dominate the hydrodynamic forces, although with reduced intensity at greater water depths (Yang, 1989). Meanwhile, the Changjiang River Estuary retreated to its modern delta region, with sediments accumulating near the coastal zones to form the delta (Figs 1b, 7c; Liu et al., 2006). As a result, the outer shelf experienced a lack of sediment supply, and a balance was reached between the tidal current field and the development of tidal sand ridges. However, the fluctuations in sea level triggered repeated ridge activities on a regional scale, leading to a mixture of young mid-late Holocene dates and older early Holocene dates. A ridge activity center developed in the southern shelf, facilitated by the thicker ridge deposits in the paleo-Changjiang River Estuary and the stronger currents (tidal and possibly internal waves) induced by the remaining funnel-shaped estuary topography.

6 Conclusions

This study aimed to investigate the formation mechanisms of seabed ridges on the ECS shelf using the core DH03 and an associated seismic profile. The ~50 m thick sandy record consisted of silty fine sands with intermittent layers of sand-mud couplets. Its benthic foraminifera assemblage was predominantly composed of offshore species. The shallow sandy strata rest on an uneven southward-sloping erosion surface that resulted from river incision during the LGM period. The thickness of the sandy sequence increased towards the south, corresponding to the topography of the basal surface. Radiocarbon dating of the core samples revealed disordered ages, with most age ranges being within recent 3 ka.

The seabed ridges, which originally formed during the early Holocene transgression, were active during the mid-late Holocene sea-level highstand. Sea-level fluctuations were indicated to trigger the ridge activities. A center for ridge activity developed in the southern shelf, facilitated by thicker ridge deposits in the paleo-Changjiang River Estuary and stronger currents induced by the remaining funnel-shaped estuary topography.

References

Amos C L, King E L. 1984. Bedforms of the Canadian eastern seaboard: a comparison with global occurrences. Marine Geology, 57(1–4): 167–208, doi: 10.1016/0025-3227(84)90199-3

Berné S, Vagner P, Guichard F, et al. 2002. Pleistocene forced regressions and tidal sand ridges in the East China Sea. Marine Geology, 188(3–4): 293–315, doi: 10.1016/S0025-3227(02)00446-2

Cao Chao, Mao Zijian, Cai Feng, et al. 2023. Dynamic geomorphology and storm response characteristics of the promontory-straight beach—a case of Gulei Beach, Fujian. Acta Oceanologica Sinica, 42(7): 64–78, doi: 10.1007/s13131-023-2225-3

Chen Zhongyuan, Saito Y, Hori K, et al. 2003. Early Holocene mud-ridge formation in the Yangtze offshore, China: a tidal-controlled estuarine pattern and sea-level implications. Marine Geology, 198(3–4): 245–257, doi: 10.1016/S0025-3227(03)00119-1

Dyer K R, Huntley D A. 1999. The origin, classification and modelling of sand banks and ridges. Continental Shelf Research, 19(10): 1285–1330, doi: 10.1016/S0278-4343(99)00028-X

Fang Xinhua, Zhang Yulin, Sun Haili, et al. 1989. An investigation of the properties of low-frequency internal waves in the northeastern China Seas. Chinese Journal of Oceanology and Limnology, 7(4): 289–299, doi: 10.1007/BF02846260

Harding A J, Arnulf A F, Blackman D K. 2016. Velocity structure near IODP Hole U1309D, Atlantis Massif, from waveform inversion of streamer data and borehole measurements. Geochemistry, Geophysics, Geosystems, 17(6): 1990–2014

Jiang Bo, Lü Xianqing. 2007. Three-dimensional numerical simulation of internal tides in the Bohai sea, the Yellow Sea and the East China sea. Transactions of Oceanology and Limnology (in Chinese), (1): 30–37

Li Jiabiao. 2008. The Regional Geology of East China Sea (in Chinese). Beijing: China Ocean Press, 85–86

Li Guangxue, Li Pin, Liu Yong, et al. 2014. Sedimentary system response to the global sea level change in the East China Seas

since the last glacial maximum. Earth-Science Reviews, 139: 390–405, doi: 10.1016/j.earscirev.2014.09.007

Li Shuanglin, Li Shaoquan, Meng Xiangjun. 2002. Chemical composition and source tracing of late Quaternary sediments in the East China Sea shelf. Marine Geology and Quaternary Geology (in Chinese), 22(4): 21–28

Liu Zhenxia, Berné S, Saito Y, et al. 2000. Quaternary seismic stratigraphy and paleoenvironments on the continental shelf of the East China Sea. Journal of Asian Earth Sciences, 18(4): 441–452, doi: 10.1016/S1367-9120(99)00077-2

Liu Zhenxia, Berné S, Saito Y, et al. 2007. Internal architecture and mobility of tidal sand ridges in the East China Sea. Continental Shelf Research, 27(13): 1820–1834, doi: 10.1016/j.csr.2007.03.002

Liu Xiaoyu, Chen Yilan, Liu Chenguang, et al. 2022. Detailed seafloor geomorphology of the western region of the North Yellow Sea, China: The result of Holocene erosional and depositional processes sculpting the offshore continental shelf. Acta Oceanologica Sinica, 41(12): 38–47, doi: 10.1007/s13131-022-2060-y

Liu Jingpu, Li Anchun, Xu Kehui, et al. 2006. Sedimentary features of the Yangtze River-derived along-shelf clinoform deposit in the East China Sea. Continental Shelf Research, 26(17–18): 2141–2156, doi: 10.1016/j.csr.2006.07.013

Liu Jian, Qiu Jiandong, Saito Y, et al. 2020. Formation of the Yangtze Shoal in response to the post-glacial transgression of the paleo-Yangtze (Changjiang) estuary, China. Marine Geology, 423: 106080, doi: 10.1016/j.margeo.2019.106080

Liu Jianxing, Shi Xuefa, Liu Qingsong, et al. 2021. Authigenic iron sulfides indicate sea-level change on the continental shelf: An illustration from the East China Sea. Journal of Geophysical Research: Solid Earth, 126(3): e2020JB021222, doi: 10.1029/2020JB021222

Liu Zhenxia, Yin Ping, Xiong Yingqian, et al. 2003. Quaternary transgressive and regressive depositional sequences in the East China Sea. Chinese Science Bulletin, 48(S1): 81–87, doi: 10.1007/BF02900944

Masson D G, Le Bas T P, Bett B J, et al. 2003. Seafloor sediments and sedimentary processes on the outer continental shelf, continental slope and basin floor. In: Strategic Environmental Assessment: SEA 4. Consultation Document. London: Department of Trade and Industry

Pico T, Creveling J R, Mitrovica J X. 2017. Sea-level records from the U. S. mid-Atlantic constrain Laurentide Ice Sheet extent during Marine Isotope Stage 3. Nature Communication, 8: 15612, doi: 10.1038/ncomms15612

Qian Jianxing. 1996. Oxygen and carbon isotope records of core DH225A in the East China Sea and their paleoceanographic significance. In: Appendix of doctoral thesis "Paleoceanographic studies of the South China Sea since the late Quaternary".

Reeder D B, Ma B B, Yang Y J. 2011. Very large subaqueous sand dunes on the upper continental slope in the South China Sea generated by episodic, shoaling deep-water internal solitary waves. Marine Geology, 279(1–4): 12–18, doi: 10.1016/j.margeo.2010.10.009

Saito Y, Katayama H, Ikehara K, et al. 1998. Transgressive and highstand systems tracts and post-glacial transgression, the East China Sea. Sedimentary Geology, 122(1–4): 217–232, doi: 10.1016/S0037-0738(98)00107-9

Snedden J W, Dalrymple R W. 1999. Modern shelf sand ridges; from historical perspective to a unified hydrodynamic and evolutionary model. In: Bergman K M, Snedden J W, eds. Isolated Shallow Marine Sand Bodies: Sequence Stratigraphic Analysis and Sedimentologic Interpretation. SEPM Special Publication, 64: 13–28

Snedden J W, Tillman R W, Culver S J. 2011. Genesis and evolution of a mid-shelf, storm-built sand ridge, New Jersey continental shelf, U. S. A. Journal of Sedimentary Research, 81(7): 534–552, doi: 10.2110/jsr.2011.26

Sun Qiliang, Wang Qing, Shi Fengyan, et al. 2022. Runup of landslide-generated tsunamis controlled by paleogeography and sea-level change. Communications Earth & Environment, 3: 244

Sun Jia, Zuo Juncheng, Huang Lin, et al. 2013. Characteristics and causes of typhoon and storm surge along coast of East China Sea. Journal of Hohai University (Natural Sciences) (in Chinese), 41(5): 461–465

Uehara K, Saito Y. 2003. Late Quaternary evolution of the Yellow/East China Sea tidal regime and its impacts on sediments dispersal and seafloor morphology. Sedimentary Geology, 162(1–2): 25–38, doi: 10.1016/S0037-0738(03)00234-3

Wang Xingxing, Kneller B, Sun Qiliang. 2023. Sediment waves control origins of submarine canyons. Geology, 51(3): 310–314, doi: 10.1130/G50642.1

Wang Zhanghua, Saito Y, Hori K, et al. 2005. Yangtze offshore, China: highly laminated sediments from the transition zone between subaqueous delta and the continental shelf. Estuarine, Coastal and Shelf Science, 62(1–2): 161–168

Wang Xingxing, Wang Yingmin, Tan Mingxuan, et al. 2020. Deep-water deposition in response to sea-level fluctuations in the past 30 kyr on the northern margin of the South China Sea. Deep-Sea Research Part Ⅰ: Oceanographic Research Papers, 163: 103317, doi: 10.1016/j.dsr.2020.103317

Wang Zhongbo, Yang Shouye, Tang Haiyan, et al. 2022. Revisit the sedimentary stratigraphic evolution and environmental changes on the outer shelf of the East China Sea since MIS 5. Frontiers in Marine Science, 9: 863245, doi: 10.3389/fmars.2022.863245

Wang Zhongbo, Yang Shouye, Wang Qiang, et al. 2014. Late Quaternary stratigraphic evolution on the outer shelf of the East China Sea. Continental Shelf Research, 90: 5–16, doi: 10.1016/j.csr.2014.04.015

Wellner R W, Bartek L R. 2003. The effect of sea level, climate, and shelf physiography on the development of incised-valley complexes: a modern example from the East China Sea. Journal of Sedimentary Research, 73(6): 926–940, doi: 10.1306/041603730926

Wu Ziyin, Jin Xianglong, Cao Zhenyi, et al. 2010. Distribution, formation and evolution of sand ridges on the East China Sea shelf. Science in China Series D: Earth Sciences, 53(1): 101–112, doi: 10.1007/s11430-009-0190-0

Wu Wei, Wang Guangxu, Lin Changsong, et al. 2023. Quantitative morphometric analysis of a deep-water channel in the Taranaki Basin, New Zealand. Acta Oceanologica Sinica, 42(5): 42–56, doi: 10.1007/s13131-022-2024-2

Xu Taoyu, Shi Xuefa, Liu Shengfa, et al. 2018. Late Quaternary sedimentary evolution of the outer shelf of the East China Sea. Quaternary International, 493: 59–69, doi: 10.1016/j.quaint.2018.06.043

Xu Taoyu, Shi Xuefa, Liu Chenguang, et al. 2020. Stratigraphic framework and evolution of the mid–late Quaternary (since marine isotope stage 8) deposits on the outer shelf of the East China Sea. Marine Geology, 419: 106047, doi: 10.1016/j.margeo.2019.106047

Yang Changshu. 1989. Active, moribund and buried tidal sand ridges in the East China Sea and the southern Yellow Sea. Marine Geology, 88(1–2): 97–116, doi: 10.1016/0025-3227(89)90007-8

Yang Shouye, Bi Lei, Li Chao, et al. 2015. Major sinks of the Changjiang (Yangtze River)-derived sediments in the East China Sea during the late Quaternary. Geological Society, London, Special Publications, 429(1): 137–152

Yang Zigeng, Wang Shengjie, Zhang Guangwei, et al. 2001. Evolution model for South Yellow Sea tidal sand ridges during transgressions in deglaciation. Marine Geology and Quaternary Geology (in Chinese), 21(3): 1–10

Yin Ping. 2003. Geomorphology and internal structure of postglacial tidal sand ridges on the East China Sea shelf. Advances in Marine Science (in Chinese), 21(2): 181–187

Yoneda M, Uno H, Shibata Y, et al. 2007. Radiocarbon marine reservoir ages in the Western Pacific estimated by pre-bomb molluscan shells. Nuclear Instruments and Methods in Physics Research Section B: Beam Interactions with Materials and Atoms, 259(1): 432–437, doi: 10.1016/j.nimb.2007.01.184

Zhang Changkuan, Zhang Dongsheng, Zhang Junlun, et al. 1999. Tidal current-induced formation-storm-induced change-tidal current-induced recovery: Interpretation of depositional dynamics of formation and evolution of radial sand ridges on the Yellow Sea seafloor. Science in China Series D: Earth Sciences, 42(1): 1–12, doi: 10.1007/BF02878492